

Physics Prospects with MeV Neutrino-Argon Charged Current Interactions using Enhanced Photon Detection in Future LArTPCs

Wei Shi,^{1,*} Xuyang Ning,² Daniel Pershey,^{3,†} Franciole Marinho,⁴
Ciro Riccio,¹ Jay Hyun Jo,² Chao Zhang,² and Flavio Cavanna⁵

¹*Stony Brook University, SUNY, Stony Brook, NY, 11794, USA*

²*Brookhaven National Laboratory, Upton, NY, 11973, USA*

³*Florida State University, Tallahassee, FL 32306, USA*

⁴*Instituto Tecnológico de Aeronautica (ITA), São José dos Campos/SP, 12228, Brasil*

⁵*Fermi National Accelerator Laboratory, Batavia, IL, 60510, U.S.A.*

(Dated: February 27, 2025)

We investigate MeV-scale electron neutrino charged current interactions in a liquid argon time projection chamber equipped with an enhanced photon detection system. Using simulations of deposited energy in charge and light calorimetry, we explore the potential for dual calorimetric neutrino energy reconstruction. We found energy reconstruction based on light-only calorimetry has a better resolution than combined charge and light calorimetry when hadrons are produced in these events. Meanwhile, enhanced light detection offers improved nanosecond timing resolution and broad optical coverage, enabling neutron tagging and identification of delayed low-energy gamma emissions. These advancements open new avenues in low-energy neutrino physics in next-generation LArTPCs.

I. INTRODUCTION

Noble liquid time projection chambers (TPCs) are widely employed for detecting rare and low-energy signals, such as neutrinos and dark matter interactions. Liquid argon (LAr) is particularly favored for its scalability and excellent tracking and calorimetric capabilities [1]. Experiments such as LArIAT [2] demonstrate sensitivity to neutrinos with energies as low as a few MeV, where electron neutrino (ν_e) charged current (CC) interactions on argon nuclei serve as the primary detection channel. These neutrinos originate from supernova bursts, solar fusion reactions, and the diffuse supernova neutrino background (DSNB) [3–5].

Argon (Ar) and xenon (Xe) emit vacuum ultra-violet (VUV) scintillation light, peaking at 127 nm and 178 nm, respectively, when charged particles deposit energy inside [6, 7]. In LArTPCs, charge signals from ionization can be collected in the presence of an electric field. The anti-correlation between charge and light signals, well-established in liquid xenon (LXe) experiments, has been used to improve energy reconstruction in searches for neutrinoless double beta decay and dark matter detection [8, 9]. In the XENON experiment, the hypothesized weakly interacting massive particle dark matter candidate would be detected through nuclear or electron recoils that deposit tens of keV energy [10, 11]. EXO-200 [8] has performed measurements of the absolute yields of charge and light in LXe for electron recoils up to MeV.

While charge detection in LArTPCs has matured [12–16], optical coverage and light yield remain limited. In

LArTPC neutrino experiments, event reconstruction primarily uses the charge signal while the light signal is mostly used to provide timing information for non-beam neutrino events. Matching charge and light signals to facilitate cosmic background rejection has been explored at MicroBooNE [17]. It is anticipated an enhanced photon detection system in future LArTPCs can offer more capabilities for physics with MeV ν_e -Ar CC interactions. The recently proposed Aluminum Profiles with Embedded X-Arapuca (APEX) [18] suggests optical coverage of up to 60% (~ 2000 m²) and an average light yield of ~ 180 photoelectrons per MeV (PE/MeV), presenting a great potential for low-energy physics.

In this work, we study the prospects of MeV neutrino physics in a LArTPC with enhanced photon detection. Key improvements include increased MeV energy resolution from light calorimetry, excellent timing resolution, and extensive optical coverage. These advancements facilitate the identification of delayed energy deposits and particle tagging, improving signal detection and background rejection, particularly in searches for the DSNB as well as many other interesting physics topics [19–26]. The insights gained in this study will guide the design and calibration of photon detection systems in future LArTPCs.

The paper is structured as follows: Sec II describes the simulation setup and energy smearing effects in LAr. Sec III details the simulated charge and light detection processes. The expected benefits of an enhanced photon detection system are discussed in Sec IV. An example application to DSNB searches is discussed in Sec V. A final summary is provided in Sec VI.

* wei.shi.1@stonybrook.edu

† dpershey@fsu.edu

II. SIMULATION

The MeV-scale ν_e CC interactions with an Ar nucleus are simulated using the MARLEY v1.2.0 event generator [27, 28]. Monoenergetic events are generated at energies ranging from 5 MeV to 50 MeV in 5 MeV increments. These events originate at the coordinate origin and propagate in the \hat{z} direction. For each energy, 1000 events are generated. The final-state particles from the neutrino interaction are tracked using Geant4 v4.10.6.p01 [29–31], interfaced via the edep-sim package [32]. The simulation is conducted in a large LAr volume, measuring 200 meters in each dimension, to ensure full containment of all simulated events. The deposited energy is recorded with a maximum step size of 0.5 cm, along with the corresponding timing information for each energy deposit.

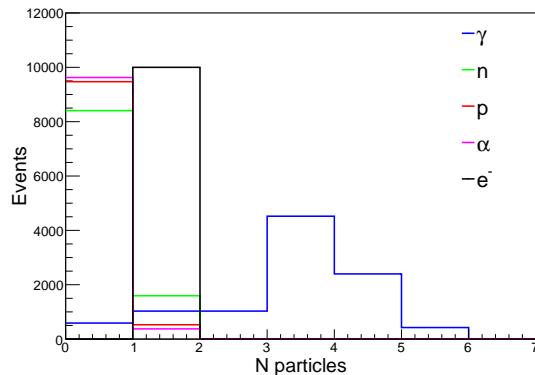


FIG. 1. Distribution of multiplicity for final state particles from ν_e -Ar CC interactions for incoming ν_e with energy in 5 - 50 MeV following a uniform distribution with mono-energetic spacing.

The multiplicity distribution of final-state particles for the MeV ν_e -Ar CC events is shown in Fig. 1. The electron carries most of the energy from the incoming ν_e and primarily loses energy through scattering, ionization, and bremsstrahlung in LAr, depending on the initial neutrino energy. The resulting electron track in the LArTPC ranges in length from sub-centimeter to tens of centimeters. Gamma rays (γ s) from the de-excitation of the final-state excited potassium-40 nucleus ($^{40}\text{K}^*$) have energies below 5 MeV. These γ s primarily lose energy through Compton scattering, pair production, and photoelectric interactions. Their energy deposits appear as blip-like objects, typically spanning a spherical region with a diameter of approximately 1 meter in the LArTPC [33]. At higher ν_e energy, one or more hadrons—primarily neutrons, protons, and α particles—can be knocked out of the Ar nucleus.

To study energy smearing, we define the available energy, E_{avail} , for outgoing final-state particles from the primary ν_e CC interaction modeled by MARLEY. For electrons and γ s, E_{avail} is defined as the particle’s total energy in the simulation. For hadrons or nuclei, E_{avail}

corresponds to their kinetic energy. The total E_{avail} of a ν_e CC event is then the sum of E_{avail} from all final-state particles.

The two-dimensional distribution of the true ν_e energy (E_{ν_e}) versus E_{avail} is shown in Fig. 2. Starting at 10 MeV, an energy loss of approximately 8 MeV due to nuclear binding energy is observed when hadrons are ejected from the Ar nucleus. This results in a secondary peak in the E_{avail} distribution, offset by 8 MeV from the primary peak (cf. Fig. 3c). Above 20 MeV, multiple hadrons can be ejected from the nucleus. Overall, hadron knock-out events constitute about 25% of all ν_e CC interactions across the 5-50 MeV range, with neutrons being the most common ($\sim 65\%$). The neutron’s 7.9 MeV binding energy escapes detection. Protons and α particles also appear in the final-state but are less common, requiring 7.6 MeV and 7.1 MeV, respectively, to overcome their binding energies. Additionally, a systematic energy shift of approximately -1 MeV is observed in the MARLEY event generator, accounting for the binding energy change from the initial Ar nucleus to the K nucleus [28]. Nuclear quenching effects on the small, keV-scale recoil energy of the daughter ^{40}K nucleus are negligible and are therefore ignored in this study.

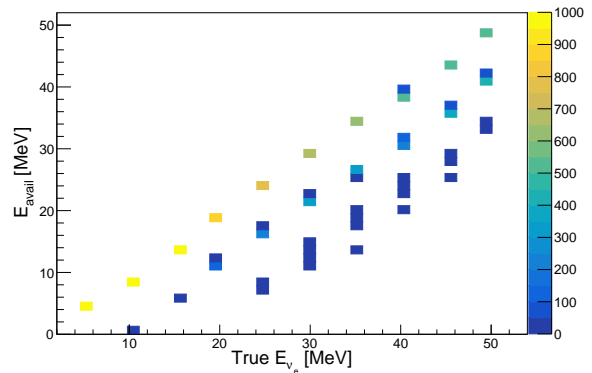


FIG. 2. Distribution of E_{avail} and true E_{ν_e} for generated ν_e -Ar CC interactions for incoming ν_e with energy in 5 - 50 MeV.

For each final-state particle interacting with the Ar nucleus, we define its deposited energy, E_{depo} , which includes energy deposition from all daughter particles involved in scattering, decay, de-excitation, etc. The primary energy smearing effect at this stage arises from neutron capture on the argon-40 (^{40}Ar) nucleus, where an additional 6.1 MeV is deposited due to the de-excitation of the resulting argon-41 (^{41}Ar) nucleus [34]. In this study, only neutron captures on ^{40}Ar are simulated, and all neutrons in the simulated events are eventually captured. The ^{41}Ar de-excitation releases several low energy gammas which may be separated out using timing and spatial information but is not considered here.

The secondary peak in the E_{avail} distribution (Fig. 3c) further splits into two smaller secondary peaks in the E_{depo} distribution. Events containing neutrons are clus-

tered approximately 1.8 MeV below the primary E_{depo} peak due to the combined effects of undetected neutron binding energy and the additional energy released from neutron capture. Furthermore, the E_{depo} of most events is shifted downward by 0.51 MeV relative to E_{avail} , corresponding to the rest mass of the final-state electron.

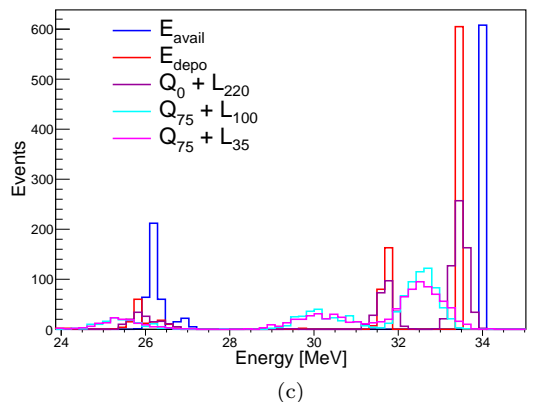
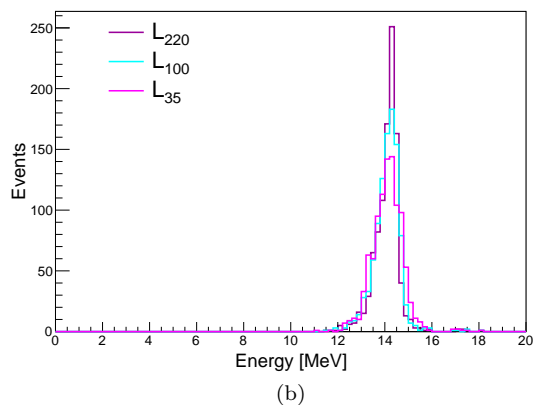
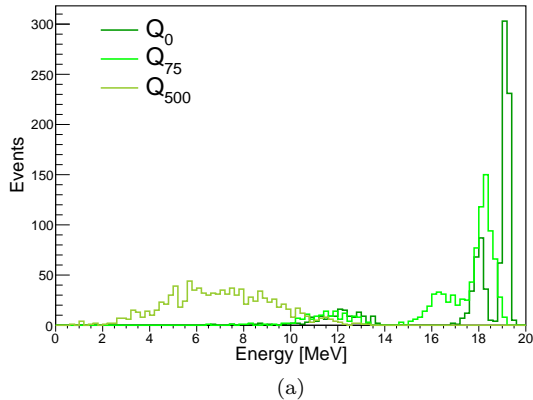


FIG. 3. Deposited energy distribution for charge (a), light (b), and combined calorimetry (c) for 35 MeV ν_e -Ar CC events.

In summary, two energy smearing mechanisms are relevant for MeV-scale ν_e CC events. The first is the hadron knockout effect from the primary ν_e -Ar interac-

tion, where a binding energy of approximately 8 MeV remains undetected in higher energy ν_e events. The second arises from the neutron capture, which introduces an additional 6.1 MeV deposition due to the γ cascade from the de-excitation of the ^{41}Ar . These two mechanisms create secondary peaks at lower E_{depo} (Fig. 3c), broadening the energy distribution and impacting low-energy physics searches.

III. CHARGE AND LIGHT DETECTION

The mechanisms for energy dissipation as charge and light in LAr have been extensively studied in previous literature [7, 35–37]. In this study, the energy deposited as charge and light is simulated using the Birks model [38], which describes the recombination of ionized electrons with noble element ions, leading to the release of additional scintillation light. For each simulated energy deposit, the corresponding linear energy transfer, dE/dx , is converted to the linear charge transfer, dQ/dx , using the following equation:

$$\frac{dQ}{dx} = \frac{dE}{dx} \times 0.83 \times R_c \quad (1)$$

Here, 0.83 is the measured fraction of deposited energy that initially undergoes ionization [39], while the recombination factor, R_c , is derived from the Birks model:

$$R_c = \frac{A}{1 + k/\epsilon \times dE/dx} \quad (2)$$

where $A = 0.8$, k is $0.0486 \frac{\text{g}}{\text{MeV cm}^2} \frac{\text{kV}}{\text{cm}}$ [40, 41]. The drift electric field, $\epsilon = 0.5 \text{ kV/cm}$, is used in this simulation.

Two charge detection thresholds, 75 keV and 500 keV, are considered and applied to the simulated charge calorimetry. The 75 keV threshold represents an optimistic detection limit, similarly used in Ref [33]. Micro-BooNE has achieved a 210 keV charge detection threshold, where the reconstruction efficiency for low energy electrons reaches 50% of its maximum achievable value in a “low-threshold” configuration on its charge collection plane [42]. The 500 keV threshold serves as a more conservative benchmark. For each energy deposit dQ , if it falls below the selected threshold, it is excluded from the charge calorimetry of the event.

The simulated energy deposited in light calorimetry, dL/dx , is defined as:

$$\frac{dL}{dx} = \frac{dE}{dx} - \frac{dQ}{dx} \quad (3)$$

where dQ comes from Eq. 1. The number of VUV photons is then simulated based on dL and the assumed light yields. We consider several benchmark detector average

\overline{LY} (PE/MeV)	35	100	140	180	220
PCE	0.16%	0.46%	0.65%	0.83%	1.01%

TABLE I. The photon collection efficiency (PCE) of five assumed average light yields.

light yields (\overline{LY}) from 35 to 220 photoelectrons per MeV of deposited energy (PE/MeV). The lower bound of 35 PE/MeV is chosen because it is close to the average light yield of the LArTPC module under construction [43]. Higher \overline{LY} values, up to 220 PE/MeV, are studied to explore what \overline{LY} future LArTPC should aim to achieve. In LAr, approximately 21622 photons are produced per MeV of deposited energy for a minimum ionizing particle (MIP) with $R_c = 0.7$ at a typical electric field of 0.5 kV/cm [35]. The overall photon collection efficiency (PCE) is defined as the ratio between the number of detected photoelectrons in the full photon detection system and the total number of photons initially produced. For each benchmark \overline{LY} , the corresponding PCE is calculated as:

$$\text{PCE}(\overline{LY}) = \overline{LY}/21622 \quad (4)$$

The PCE values for five benchmark \overline{LY} are listed in Table I.

The simulated expected average number of produced photons, \overline{N}_{ph} , in LAr is:

$$\overline{N}_{\text{ph}} = \frac{dL}{19.5 \text{ eV}} \times \text{PCE} \quad (5)$$

where 19.5 eV is the average energy required to produce a single 127 nm photon in LAr [39]. The detected number of photoelectrons, N_{PE} , is simulated by applying Poisson smearing:

$$N_{\text{PE}} = \text{Poisson}(\overline{N}_{\text{ph}}, \sqrt{\overline{N}_{\text{ph}}}) \quad (6)$$

The final detected energy deposited in light is then derived from the detected photoelectrons:

$$L_{\overline{LY}} = \frac{N_{\text{PE}} \times 19.5 \text{ eV}}{\text{PCE}(\overline{LY})} \quad (7)$$

Fig. 3 shows the distributions of deposited charge and light from 35 MeV ν_e CC interactions on Ar. In addition to E_{avail} and E_{depo} described in Sec. II, the energy deposited as charge at zero charge detection threshold, Q_0 , primarily peaks around 19 MeV (Fig. 3a). Secondary peaks in the Q_0 distribution originate from E_{depo} due to events with knockout hadrons. The secondary peak at 18 MeV in Q_0 corresponds to events with neutron emission, while the broader peak at 12 MeV consists of events with a proton or an α particle. Compared to

E_{depo} , the Birks model introduces additional broadening in Q_0 . This broadening is more pronounced for secondary peaks because knockout hadrons are not MIPs, leading to greater variation in recombination effects as described by the Birks model.

Applying a charge detection threshold of 75 keV further broadens the deposited charge calorimetry, Q_{75} , relative to Q_0 , and introduces a negative energy bias. The 500 keV threshold significantly smears the charge calorimetry distribution, Q_{500} , reducing the precision of energy reconstruction.

For energy deposited as light, the events are centered around 14 MeV (Fig. 3b). The secondary peaks are less distinct and merge with the primary peak. This effect is further illustrated in Fig. 4, which shows the energy deposited in light for $\overline{LY} = 220$ PE/MeV (L_{220}). Specifically, for events with neutrons, the net bias in deposited energy is -1.8 MeV. The total deposited energy of these events typically fall within the two-standard-deviation band of the primary light peak. Consequently, neutron emission events populate the lower tail of the L_{220} distribution in Fig. 4 rather than forming a distinct secondary peak, as observed in the charge distribution.

It is important to note that nuclear quenching effects in hadron-nucleus interactions are not explicitly simulated in this study. In particular, a lower scintillation efficiency has been observed in tens of keV nuclear recoils in LXe [44]. For α particles, a smaller light yield is observed possibly explained by a biexcitonic quenching process; while for few MeV protons, this was calculated to be negligible [45]. For neutrons in this study, the potential extra light loss could shift neutron emission events further from the primary peak in the light distribution.

The single peak structure of the light distribution is observed across all ν_e samples from 5 to 50 MeV and holds true for all benchmark \overline{LY} . Unlike the charge calorimetry, no systematic energy bias is introduced when varying \overline{LY} . However, energy smearing effects become more pronounced as \overline{LY} decreases from 220 PE/MeV to 35 PE/MeV.

Finally, the event E_{depo} is largely recovered when combining charge and light calorimetry, $Q_0 + L_{220}$ (Fig. 3c). Similar to charge-only calorimetry, the application of a 75 keV charge detection threshold introduces spectral broadening and an energy bias in the combined calorimetry. Additionally, implementing the modified Box model[46] to simulate recombination effects yields similar results to those obtained using the Birks model.

IV. CAPABILITIES FROM ENHANCED LIGHT DETECTION

A. Energy Reconstruction

In this section, we examine the potential for energy reconstruction using charge and light calorimetry in a future LArTPC with an enhanced photon detection sys-

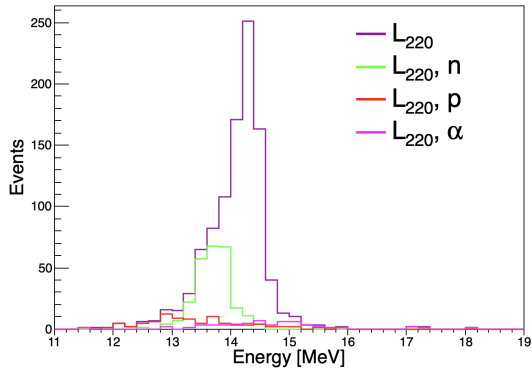


FIG. 4. Deposited energy in light assuming $\overline{LY} = 220$ PE/MeV for 35 MeV ν_e -Ar CC events (purple), overlaid with distribution of events with knockout neutrons (green), protons (red), and α s (pink).

tem. The E_{avail} for ν_e CC events can be reconstructed by applying a scaling factor to the deposited energy. The scaling factor represents the fraction of E_{avail} that is converted into deposited energy in charge, light, or combined calorimetry in each event.

As an example, we consider charge calorimetry with a detection threshold of 75 keV, Q_{75} . From simulation, we determine a scale factor of 0.54, taken as the mode of the ratio distribution between Q_{75} and E_{avail} . The reconstructed energy from Q_{75} is then given by:

$$E_{\text{reco}, Q_{75}} = Q_{75}/0.54 \quad (8)$$

Similarly, the event energy can be reconstructed using the total deposited energy in light, for instance, with an assumed $\overline{LY} = 220$ PE/MeV:

$$E_{\text{reco}, L_{220}} = L_{220}/0.42 \quad (9)$$

Alternatively, the ν_e event energy can be reconstructed by combining charge and light calorimetry:

$$E_{\text{reco}, Q_{75} + L_{220}} = (Q_{75} + L_{220})/0.96 \quad (10)$$

The energy distributions obtained using these three reconstruction methods for 35 MeV ν_e -Ar CC events are shown in Fig. 5. Notably, the combined charge and light energy reconstruction (Eq. 10) results in a narrower distribution than charge-only reconstruction (Eq. 8). Although secondary peaks, inherited from the charge-only energy distribution, remain present, the primary peak in the combined calorimetry distribution is significantly narrower than that of the light-only reconstruction (Eq. 9).

These results come from the intrinsic anti-correlation between charge and light signals for MeV-scale ν_e -Ar CC

events, previously also observed in liquid xenon (LXe) experiments [8, 9]. The excellent energy resolution achieved by the combined calorimetry for events without knockout hadrons is further detailed in Appendix A.

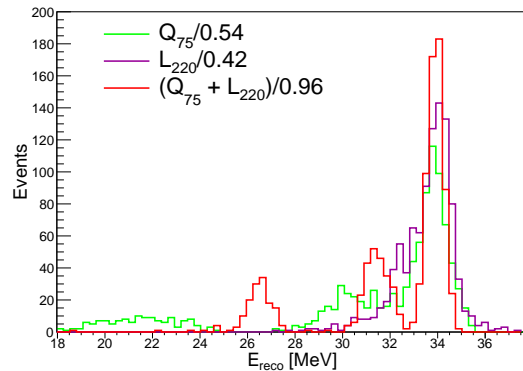


FIG. 5. Reconstructed E_{avail} for 35 MeV ν_e -Ar CC events using charge only (green), light only (purple), and combined charge and light energy deposits (red).

Energy reconstruction using the three methods is performed for all simulated samples from 5 MeV to 50 MeV under the optimistic 75 keV charge detection threshold and across all benchmark \overline{LY} . Since the light only distribution is non-Gaussian and both the charge-only and combined calorimetry distributions exhibit multiple secondary peaks, we use the histogram standard deviation (σ_h) and mean (\overline{E}_h) to characterize the energy smearing and calculate the energy resolution.

Fig. 6 shows the energy resolution as a function of true E_{ν_e} and as a function of \overline{LY} for the 20 MeV ν_e sample, using the full statistics of the simulated dataset. For ν_e energies below 15 MeV, the combined calorimetry method provides the best energy resolution among the three reconstruction approaches for any benchmark \overline{LY} . This improvement is attributed to the intrinsic anti-correlation between charge and light signals, as demonstrated in Appendix A.

As ν_e energy increases, the fraction of hadron emission events rises, leading to a larger standard deviation in the reconstructed energy for all three methods and causing a degradation in energy resolution. However, above 25 MeV, the impact of undetectable binding energy from hadron emission becomes relatively small compared to the total neutrino event energy, and the energy resolution is no longer dominated by these effects. Compared to the charge-only reconstruction, the light-only reconstruction is less affected by hadron emission events, maintaining a nearly flat energy resolution as a function of true neutrino energy. This stability arises from the absence of secondary peaks, as shown in Fig. 4.

For ν_e energies above 15 MeV, light-only reconstruction provides the best energy resolution. Although not explicitly shown here, this trend is consistent across all five benchmark \overline{LY} scenarios for ν_e energies above 20

MeV. While combined calorimetry still improves the energy resolution relative to charge-only reconstruction, it largely inherits the resolution behavior of the charge-only method.

For the 20 MeV ν_e sample shown in the bottom plot of Fig. 6, the energy resolution of the light-only method improves as \overline{LY} increases. It also outperforms both charge-only and combined calorimetry reconstruction across all benchmark \overline{LY} , a trend that holds for ν_e energies above 15 MeV. The combined calorimetry method does not show significant improvement in energy resolution at higher \overline{LY} , as its performance remains dominated by charge calorimetry. This study demonstrates that, given sufficient light collection, light-only reconstruction can achieve superior energy resolution compared to traditional charge-based calorimetry.

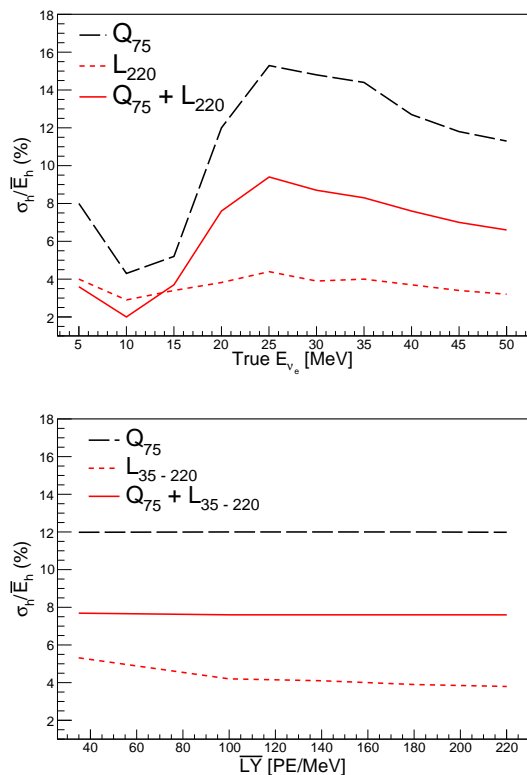


FIG. 6. Reconstructed energy resolution for all events in each ν_e energy sample. Top: reconstructed event energy resolution as a function of true E_{ν_e} from 5 to 50 MeV. Bottom: reconstructed energy resolution as a function of benchmark \overline{LY} for 20 MeV ν_e .

B. Hadron Tagging

Beyond the improvements in energy reconstruction achieved through light calorimetry and dual calorimetry, further enhancement in energy resolution is expected from the ability to tag hadrons in future LArTPCs with

advanced light detection systems. In particular, tagging delayed energy deposits from neutrons and their captures using timing information from the photon detection system can significantly reduce energy smearing. An example of a simulated ν_e -Ar CC event display is shown in Fig. 7. While the variation in dE/dx is relatively small across all energy deposits, the timing domain reveals key distinguishing features. Fast timing capabilities and extensive photodetector coverage in LArTPCs can help separate energy deposits from electromagnetic activities (occurring within 10 ns) and neutron scattering activities (which extend up to a few μ s). In the case of neutron capture, the capture time is primarily determined by capture on the most abundant ^{40}Ar isotope and is expected to be on the order of $\mathcal{O}(100)$ μ s. The energy from the cascade gamma-rays adds up to 6.1 MeV and can be identified by the photon detection system and correlated with the primary interaction.

For this study, we assume that two common hadrons knocked out of the Ar nucleus in MeV-scale ν_e CC interactions—protons and α particles—can be tagged when their deposited charge energy exceeds the optimistic 75 keV threshold. Under this assumption, the hadron tagging efficiency is 84% for protons and 18% for α particles across all simulated neutrino events in the 5–50 MeV range. In the simulation, all neutrons are captured on ^{40}Ar , and we assume all captured neutrons can be tagged in this study.

The decision to include or exclude events with tagged hadrons depends on the specific signal and background considerations of a given analysis. Here, we explore both possibilities. When including these tagged events in the reconstructed sample, we apply an energy correction by adding back an average binding energy of 7.35 MeV for each tagged proton or α , and 7.9 MeV for each tagged neutron, while subtracting 6.1 MeV to account for the neutron capture on ^{40}Ar . To exclude the hadron tagged events, they are simply discarded.

Fig. 8 illustrates both approaches for the 35 MeV ν_e -Ar CC simulated sample using the combined calorimetric reconstruction from Eq. 10. The figure clearly shows that all neutron-containing events in the 30–32 MeV range are tagged, and they can either be incorporated into the primary peak at 34 MeV or removed. Events with a proton or an α cluster below 28 MeV and approximately 60% of them are tagged in the 35 MeV ν_e sample. The total tagging efficiency for protons and α particles exceeds 50% for ν_e above 20 MeV.

The energy resolution after hadron tagging (σ_h/\bar{E}_h) is shown in Fig. 9 for both cases: including and excluding the tagged events. Hadron tagging significantly improves the energy resolution for the combined calorimetry reconstruction. For example, in the 25 MeV sample, the energy resolution improved from 9.4% to 5.8%. Above 25 MeV, including tagged events results in only a marginal improvement over excluding them. Meanwhile, light-only reconstruction continues to provide the best energy resolution for all ν_e samples above 20 MeV.

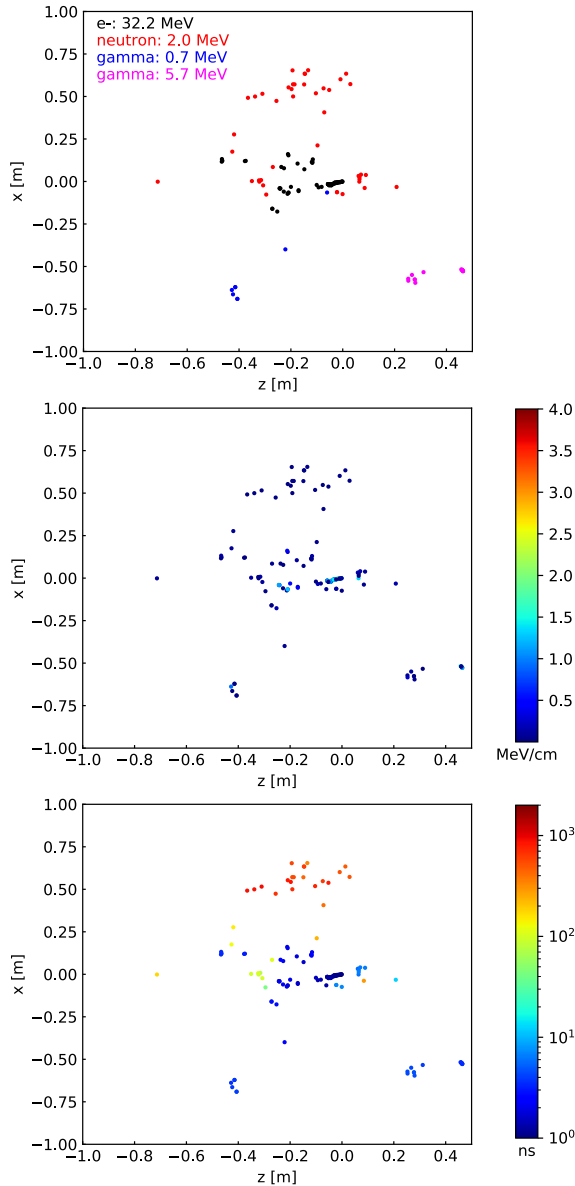


FIG. 7. Displays of simulated energy deposits from a 50 MeV ν_e -Ar CC event. The event vertex is located at the origin (0, 0, 0). The energy deposits are color-coded based on final state particles (top), linear energy transfer dE/dx (middle), and energy deposit time (bottom) respectively.

For the 20 MeV ν_e sample shown in the bottom plot of Fig. 9, post-hadron-tagging combined calorimetry achieves an energy resolution comparable to that of light-only reconstruction across all benchmark \overline{LY} .

We note that, according to Fig. 3 and Fig. 4, one should avoid making the same correction to the reconstructed energy based on tagged hadrons in the light-only or charge-only energy reconstruction. This is due to large event-by-event fluctuations in dE/dx for emitted hadrons, which affect the partitioning of energy between charge and light calorimetry according to the Birks

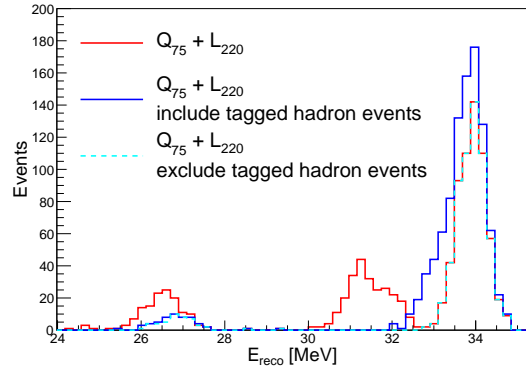


FIG. 8. Reconstructed E_{avail} for 35 MeV ν_e -Ar CC events with combined charge and light calorimetry before and after hadron tagging.

model. Additionally, explicit charged particle identification (PID) of electrons or γ s does not further enhance the reconstructed energy resolution, as energy smearing at the deposition stage is already minimal for these particles.

C. Tagging Delayed Gamma in ν_e -Ar CC Interactions

The ν_e -Ar CC cross section receives contributions from both Fermi and Gamow-Teller transitions [28, 47–49]. Approximately 65% of Fermi transitions in Ar involve delayed γ emission due to a long-lived intermediate nuclear state of the daughter $^{40}\text{K}^*$ nucleus [50]. In these interactions, the nucleus is initially excited to 4.38 MeV and subsequently deexcites via a prompt 2.73 MeV γ emission, followed by a delayed 1.65 MeV γ emission. The delayed 1.65 MeV γ is associated with a characteristic decay time of 480 ns, resulting in a distinctive two-pulse timing structure in the light signal, which can be identified using the photon detection system. The reconstruction of these low energy γ s could be further strengthened by detailed blip reconstruction techniques, as demonstrated in Ref [33].

High- \overline{LY} photon detection in LArTPCs, such as that achievable with the APEX design [18], can significantly reduce radiological background by requiring coincident activities. This is made possible by the favorable energy, vertex, and time resolution of the light signal. An application of these capabilities in solar neutrinos is possible. These studies are ongoing and will be reported later. We briefly mention potential impact here:

Improved vertex reconstruction: with large background rates from external and internal radioactivity, matching low-energy charge and light deposits is difficult in a large LArTPC. Vertex reconstruction is ~ 1 cm for charge and limited by the light signal. Increased light collection efficiency improves vertex resolution which in turn will im-

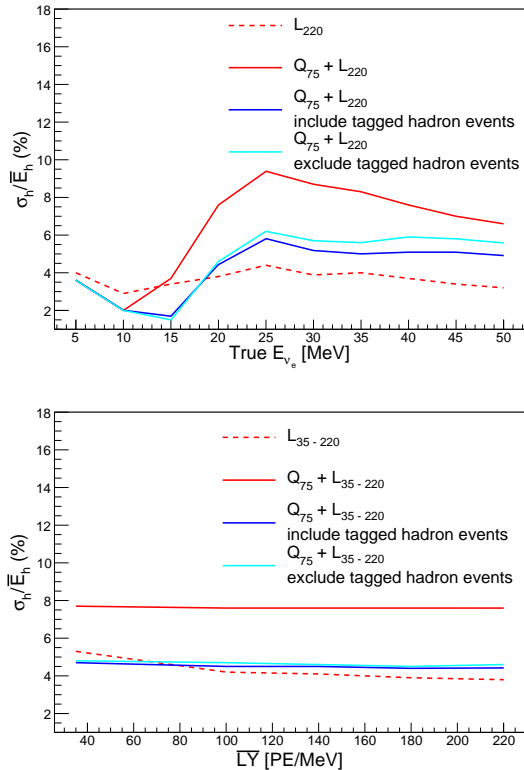


FIG. 9. Reconstructed energy resolution for all events in each ν_e energy sample after hadron tagging. Both options of including and excluding tagged hadron events are shown. Top: reconstructed event energy resolution as a function of true E_{ν_e} from 5 to 50 MeV. Bottom: reconstructed energy resolution as a function of benchmark \overline{LY} for 20 MeV ν_e .

prove the matching efficiency. This is crucial for rejecting γ backgrounds produced in the rock surrounding the LArTPC.

Fermi transition tagging: Separating Fermi transition interactions that emit a 1.65 MeV delayed gamma from Gamow-Teller signal and radiological background would impact solar neutrino analysis and supernova pointing in LArTPC detectors. Searching for two flashes, possible through improved energy and vertex reconstruction, would dramatically reduce backgrounds from natural radioactivity and neutron capture for solar neutrino measurements. For a supernova neutrino burst, these selected events would also have improved energy resolution as no nucleons are emitted in Fermi transitions. Fermi and Gamow-Teller interactions also have different angular distributions for final state leptons: $1 + \cos \theta_e$ and $1 - \frac{1}{3} \cos \theta_e$ respectively [27]. If Fermi transitions could be tagged on an event-by-event basis, their angular dependence would give additional information on pinpointing the supernova for optical followup [47].

V. APPLICATIONS TO LOW ENERGY PHYSICS

The energy reconstruction incorporating the light calorimetry and the assumed hadron tagging capability described in Sec IV are applied to the DSNB search as an example physics application. To refine energy smearing, the energy granularity of the Monte Carlo samples described in Sec II is enhanced by adding additional mono-energetic ν_e events from 5 MeV to 80 MeV in 0.5 MeV increments. For each energy step, 1000 events are generated and simulated. The final energy smearing matrices are shown in Fig. 13 in Appendix B.

The DSNB represents the cumulative neutrino flux from all core-collapse supernovae out to several Gpc that arrives at Earth [51]. It is a guaranteed yet undiscovered signal. LArTPC experiments offer an unique capability to constrain the ν_e flux, complementing other next-generation neutrino experiments such as JUNO [52] and Hyper-Kamiokande [53], which are more sensitive to the $\bar{\nu}_e$ flux. The observation and measurement of DSNB would provide critical insights into the local supernova density and the relative DSNB contribution from black hole- and neutron star-forming supernovae.

Fig. 10 shows the expected DSNB spectra at arbitrary exposure using the $E_{\text{reco}}, Q_{75} + L_{180}$ smearing, assuming a LArTPC module with enhanced photon detection, including the hadron tagging capability as described in Sec. IV B. Here we choose to show the event rates in arbitrary exposures to highlight the signal and background spectra and avoid explicitly deriving sensitivities for specific exposures. The vertical axis represents normalized event rates and does not correspond to actual event counts. The assumptions for the DSNB ν_e flux model follow those in Ref. [51]. The solar ν_e flux is derived from well-known nuclear cross-section measurements [54], with oscillations applied using parameters $\Delta m_{12}^2 = 4.86 \times 10^{-5} \text{eV}^2$ and $\sin^2 \theta_{12} = 0.306$. Although the Δm_{21}^2 value used is slightly outdated, its impact on the results is negligible. The atmospheric ν_e flux is taken from Ref. [4] assuming the detector is at the SURF site.

The DSNB signal is primarily constrained to a narrow energy region of interest (ROI). At the lower end of this ROI, the dominant background comes from the intense solar ${}^3\text{He-p}$ and ${}^8\text{B}$ ν_e fluxes, while at the higher end, atmospheric neutrino backgrounds gradually increase. Notably, the atmospheric ν_e flux below ~ 100 MeV remains uncertain, making sensitivity optimization in the lower-energy bins within the ROI crucial.

For solar backgrounds, energy smearing caused by the secondary peak from hadron knockout effects (as described in Sec IV B) does not impact the DSNB search. The primary reconstructed energy peak from combined charge and light calorimetry, shown in Fig. 12 in Sec IV A, provides the best opportunity to improve the search sensitivity. Conversely, for atmospheric background at the high-energy bins of the DSNB ROI, the secondary peak does affect the search sensitivity. There-

fore, tagging ν_e CC events with knockout hadrons is crucial to mitigating smearing effects. Alternatively, one can rely on light-only energy reconstruction, which achieves better energy resolution above 20 MeV than combined calorimetry post hadron tagging, as demonstrated in Fig. 9.

To evaluate the impact of different reconstruction approaches, we apply energy smearing matrices from five reconstruction strategies: charge-only, light-only, combined calorimetry, and combined calorimetry with and without tagged hadron events, using all benchmark \overline{LY} .

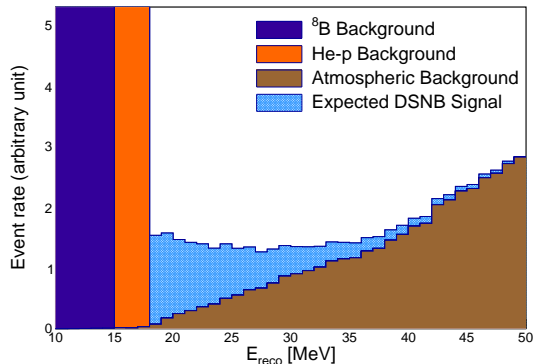


FIG. 10. Expected DSNB spectra with backgrounds at an arbitrary exposure under the best energy reconstruction strategy of combined calorimetry at a \overline{LY} of 180 PE/MeV, $E_{\text{reco}}, Q_{75} + L_{180}$, and exclusion of hadron tagged events. The event rate on the vertical axis uses an arbitrary unit after normalization and doesn't represent actual number of events.

To compare the performance of different energy reconstruction methods, the $-2\log\text{-likelihood}$ of the DSNB search (shown in Fig. 10) is defined and calculated for 400 kt-yr exposure:

$$-2\log\text{-likelihood} = 2 \sum_i (E_i - O_i + O_i \times \log \frac{O_i}{E_i}) \quad (11)$$

where i runs over all bins in the energy ROI, E_i represents the expected background in the i^{th} energy bin, and O_i is the sum of signal and background in the same bin.

The best DSNB search sensitivity from different energy reconstruction strategies is shown in Fig. 11 as a function of the upper bound of the energy ROI, with the lower bound fixed at 18 MeV in all cases. The light-only reconstruction, assuming a benchmark \overline{LY} of 180 PE/MeV (L_{180}), achieves a higher plateau sensitivity than the charge-only reconstruction, which assumes an optimistic 75 keV charge detection threshold (Q_{75}). However, Q_{75} yields better sensitivity at the lower-energy end of the ROI compared to L_{180} , as the secondary peaks in charge-only reconstruction smear the solar background to even lower energies, shifting it outside the DSNB ROI.

Energy reconstruction using combined calorimetry provides a slight improvement in plateau sensitivity.

However, when combined with the hadron tagging capability described in Sec.IV B, it achieves the highest plateau sensitivity. Hadron tagging is particularly beneficial at higher-energy ROIs, where atmospheric background dominates. The inclusion or exclusion of tagged hadron events has minimal impact on sensitivity, so only one result is presented in Fig.11. Additionally, for \overline{LY} above 180 PE/MeV, no significant improvement in sensitivity is observed for light-only, combined calorimetry, or combined calorimetry with tagged hadron events, as energy resolution is no longer the limiting factor.

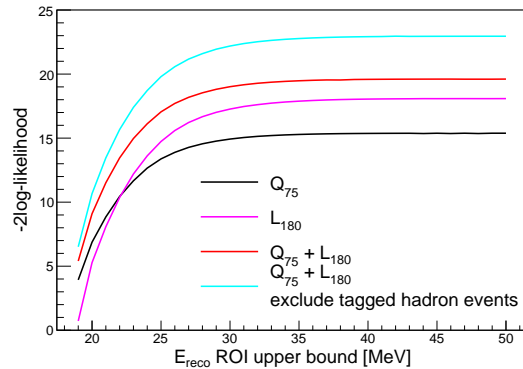


FIG. 11. Expected DSNB sensitivities $-2\log\text{-likelihood}$ for 400 kt-yr exposure under different energy reconstruction strategies.

Further improvements in DSNB sensitivity could be achieved by tagging solar ν_e backgrounds using the directionality of final-state electrons in Fermi transitions, as described in Sec IV C. This would allow statistical separation between directional solar events and the isotropic DSNB signal, enabling the ROI to be extended to lower energies and thereby increasing the DSNB event rate. Additionally, the broad energy range and baseline coverage of atmospheric neutrino oscillations in future LArTPC experiments could help constrain sub-GeV atmospheric neutrino fluxes [55].

VI. SUMMARY AND OUTLOOK

We studied MeV ν_e -Ar CC interactions and simulated the energy deposit into charge and light signals. At the generator level, an energy smearing effect is observed from hadron emission whose associated binding energy is undetectable. The dominant energy smearing at the energy deposition stage in LAr comes from neutron captures on Ar nuclei. Therefore for low energy physics it is important to tag hadron multiplicities. Further hadron PID, especially the tagging of neutrons as they are the primary knockout hadrons from these interactions according to MARLEY simulation, can help precisely correct for the energy smearing effect from neutron. The identification of protons and α s is possible by looking

for highly localized collected charge since these hadrons have high dE/dx and are expected to only span ~ 1 cm in the charge readout views in LArTPCs. It is promising that neutron captures can be tagged by a combined analysis of signals from both the charge and light detection systems in LArTPC through blips analysis and timing information [33, 56]. Developing techniques for tagging MeV neutrons and delayed neutron captures on Ar nucleus at smaller scale LArTPCs utilizing information from both the charge and the light detection systems will be interesting.

An energy reconstruction based on light only calorimetry, or a combine calorimetry assuming an optimistic 75 keV charge detection threshold and average light yield of 180 PE/MeV, both show excellent energy resolution when compared to charge-only energy reconstruction. In particular, for tens of MeV ν_e -Ar CC events, we found the energy reconstructed based on light-only calorimetry has a better resolution than combined charge and light calorimetry when hadron emission events are included. The improved energy resolution from the combined charge and light calorimetry boosts the DSNB discovery potential compared to an optimistic charge based reconstruction at the same exposure without taking into account systematic uncertainties. Once the hadron emission events are tagged, the combined calorimetry offers the best achievable DSNB sensitivity.

This study offers insights into implementing energy reconstruction using combined charge and light calorimetry. According to Eq. 7, the deposited energy in light is derived from the detected photoelectrons and also the overall PCE of the LArTPC. For MeV neutrino events which have energy deposits spread over a sphere of ~ 50 cm, the collected photoelectrons can be easily calculated by summing up detected photoelectrons from all photodetectors. In reality, the PCE of the LArTPC varies as a function of position. It's expected light calorimetry calibration at a voxel size of 50 cm can be achieved where the LY is reasonably uniform. With the precise position information reconstructed from both the charge and the light detection systems, Eq. 4 can be used to obtain the PCE for the voxel where the MeV interaction happens. The energy deposited in charge shown in Eq. 1 can be obtained based on calculations in Ref [35]. Furthermore, for a homogeneous calorimeter such as LAr, the uncertainty associated with the light calorimetry calibration itself is expected to contribute as a constant term to the overall energy resolution budget [1]. The excellent energy resolution achieved from the dual calorimetry in this study also requires superb signal-to-noise ratio in both the charge and light readout systems of the LArTPC.

The excellent light collection capability from extensive coverage and nanosecond timing resolution will also reduce solar neutrino analysis thresholds in a LArTPC by requiring a coincidence of pulses expected in a golden channel in the daughter $^{40}\text{K}^*$ deexcitation leading to very low background solar neutrino samples. The background rejection using coincident light signals should be tested

with a robust model of photon simulation in a LArTPC. Furthermore, a better understanding of the scintillation reconstruction is needed, including vertex resolution from light topology and timing. Reconstruction of the delayed γ pulse also requires a precise knowledge of the scintillation time profile (with or without Xe deoping). The lifetime of the ^{40m}K state, 480 ns, is short compared to the few- μs primary pulse. Therefore pulse-shape discrimination will be critical for identifying the two-pulse structure. How this affects energy and vertex resolution must also be studied.

Throughout this work, the nonuniformity of the light yield in the photon detection system is not considered, but is expected to affect both physics analyses. Nevertheless, this study provides guidance to the realization of an enhanced photon detection system in future LArTPCs with high and uniform light yield. Furthermore, this work will motivate the development of more sophisticated techniques and analyses utilizing both the charge and the light detection systems in future LArTPCs to realize these low energy physics prospects.

ACKNOWLEDGMENTS

We are grateful to have L. Strigari and Y. Zhuang from TAMU provide the latest estimated SURF atmospheric flux. We thank E. Church, E. Granados-Vazquez, C. Jung, X. Qian, J. Reichenbacher, K. Scholberg, and L. Wan for their insightful discussions on the studies presented in this paper. This work is supported by 2024 SBU-BNL Seed Grant Program and BNL LDRD 23-058.

Appendix A: Energy Resolution for MeV ν_e -Ar CC Events without Hadron Emission

To highlight the improvement in energy resolution provided by combined calorimetry for neutrino events without hadrons, we fit a Gaussian function to the primary reconstructed energy peak, excluding events with hadron emissions. We use the fitted standard deviation (σ_G) and mean energy (\bar{E}_G) to quantify the energy resolution. The energy resolution as a function of true E_{ν_e} and as a function of \bar{LY} for the 20 MeV ν_e sample is shown in Fig. 12, based on the Gaussian-fitted primary peak.

In Fig. 12, for the 35 MeV ν_e -Ar CC sample, the combined calorimetry achieves an energy resolution 1.0% ($5.9\%/\sqrt{E}$), compared to 1.9% ($11.3\%/\sqrt{E}$) for charge-only calorimetry. For the primary peak of events without hadrons, the energy resolution of the light-only reconstruction at $\bar{LY} = 220$ PE/MeV already surpasses that of charge-only reconstruction across true E_{ν_e} range of 5-50 MeV. Although not shown here, this trend also holds for \bar{LY} above 140 PE/MeV. The combined calorimetry further improves the energy resolution across the same energy range.

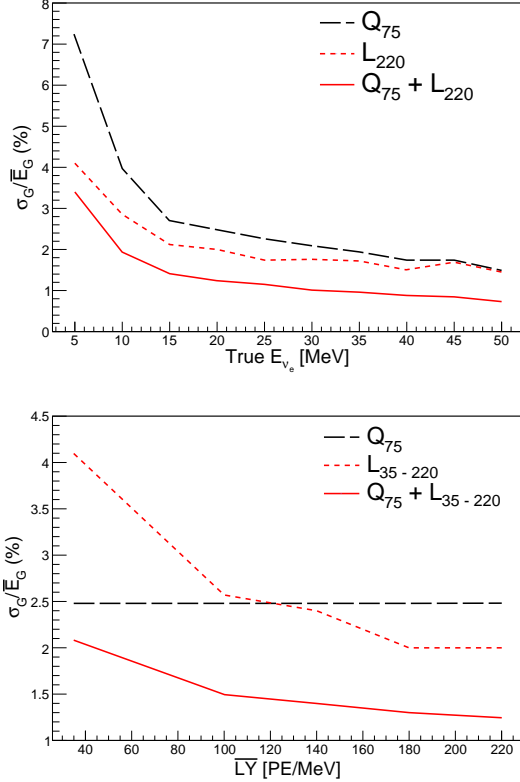


FIG. 12. Reconstructed energy resolution for the primary peak containing only events without hadrons. Top: reconstructed E_{avail} resolution as a function of true E_{ν_e} from 5 to 50 MeV. Bottom: reconstructed E_{avail} resolution as a function of benchmark \overline{LY} for 20 MeV ν_e .

For the 20 MeV ν_e sample shown in the bottom plot of Fig. 12, the energy resolution of the light-only reconstruction $E_{\text{reco}, L_{220}}$ is 2.0% ($8.8\%/\sqrt{E}$), while the resolution from charge-only calorimetry $E_{\text{reco}, Q_{75}}$ is 2.5% ($10.8\%/\sqrt{E}$). When \overline{LY} exceeds 100 PE/MeV, the energy resolution of light-only calorimetry (dotted lines) is comparable or better than that of charge-only calorimetry $E_{\text{reco}, Q_{75}}$ (dashed line). Furthermore, across all benchmark \overline{LY} scenarios, combined charge and light

calorimetry improves energy resolution by approximately a factor of two compared to charge-only or light-only reconstruction. This enhancement is attributed to the intrinsic anti-correlation between charge and light signals.

Most importantly, with a significantly higher \overline{LY} above 100 PE/MeV the reconstructed energy resolution can be up to twice as good as that in the 35 PE/MeV scenario, whether using light-only reconstruction or combined charge and light reconstruction.

Appendix B: Energy Smearing Matrices

Fig. 13 shows 2D energy response matrices of reconstructed neutrino energy vs. true neutrino energy for electron neutrinos. The reconstructed energy comes from the charge-only deposited energy with 75 keV detection threshold, Q_{75} (top left), light-only L_{180} (top right), combined charge and light deposited energy for $\overline{LY} = 180$ PE/MeV, $Q_{75} + L_{180}$, without (bottom left), and with (bottom right) hadron tagged events removed.

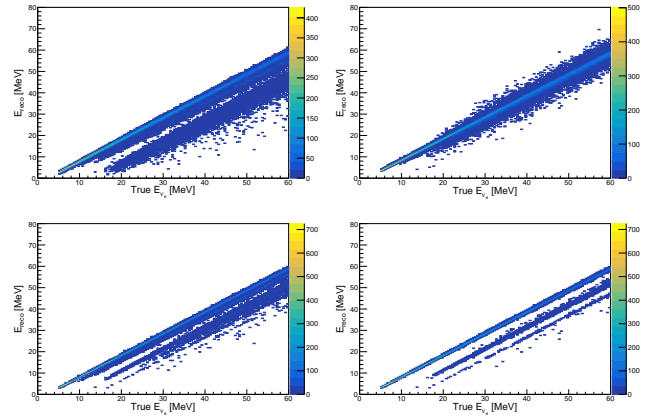


FIG. 13. Energy response matrices of reconstructed neutrino energy vs. true neutrino energy for electron neutrinos. The reconstructed energy comes from the charge-only deposited energy with 75 keV detection threshold, Q_{75} (top left), light-only L_{180} (top right), combined charge and light deposited energy for $\overline{LY} = 180$ PE/MeV, $Q_{75} + L_{180}$, without (bottom left), and with (bottom right) hadron tagged events removed.

[1] C. W. Fabjan and F. Gianotti, Calorimetry for particle physics, *Rev. Mod. Phys.* **75**, 1243 (2003).
 [2] W. Foreman *et al.* (LArIAT Collaboration), Calorimetry for low-energy electrons using charge and light in liquid argon, *Phys. Rev. D* **101**, 012010 (2020).
 [3] C. A. J. O’Hare, Dark matter astrophysical uncertainties and the neutrino floor, *Phys. Rev. D* **94**, 063527 (2016).
 [4] Y. Zhuang, L. E. Strigari, and R. F. Lang, Time variation of the atmospheric neutrino flux at dark matter detectors, *Phys. Rev. D* **105**, 043001 (2022).

[5] B. Zhou and J. F. Beacom, First detailed calculation of atmospheric neutrino foregrounds to the diffuse supernova neutrino background in Super-Kamiokande, *Phys. Rev. D* **109**, 103003 (2024).
 [6] J. Jortner, L. Meyer, S. A. Rice, and E. G. Wilson, Localized Excitations in Condensed Ne, Ar, Kr, and Xe, *The Journal of Chemical Physics* **42**, 4250 (1965), https://pubs.aip.org/aip/jcp/article-pdf/42/12/4250/18838475/4250_1_online.pdf.

- [7] E. Segreto, Properties of liquid argon scintillation light emission, *Phys. Rev. D* **103**, 043001 (2021).
- [8] G. Anton *et al.* (EXO-200 Collaboration), Measurement of the scintillation and ionization response of liquid xenon at MeV energies in the EXO-200 experiment, *Phys. Rev. C* **101**, 065501 (2020).
- [9] E. Aprile *et al.* (XENON Collaboration), The XENON100 dark matter experiment, *Astroparticle Physics* **35**, 573 (2012).
- [10] E. Aprile *et al.* (XENON Collaboration), First Dark Matter Search with Nuclear Recoils from the XENONnT Experiment, *Phys. Rev. Lett.* **131**, 041003 (2023).
- [11] E. Aprile *et al.* (XENON Collaboration), Search for New Physics in Electronic Recoil Data from XENONnT, *Phys. Rev. Lett.* **129**, 161805 (2022).
- [12] R. Acciarri *et al.* (MicroBooNE), Design and Construction of the MicroBooNE Detector, *JINST* **12** (02), P02017, arXiv:1612.05824 [physics.ins-det].
- [13] S. Amerio *et al.* (ICARUS-T600), Design, construction and tests of the ICARUS T600 detector, *Nucl. Instrum. Meth. A* **527**, 329 (2004).
- [14] L. Bagby *et al.* (ICARUS), Overhaul and Installation of the ICARUS-T600 Liquid Argon TPC Electronics for the FNAL Short Baseline Neutrino Program, *JINST* **16** (01), P01037, arXiv:2010.02042 [physics.ins-det].
- [15] R. Acciarri *et al.* (SBND), Construction of precision wire readout planes for the Short-Baseline Near Detector (SBND), *JINST* **15** (06), P06033, arXiv:2002.08424 [physics.ins-det].
- [16] A. A. Abud *et al.* (DUNE), Design, construction and operation of the ProtoDUNE-SP Liquid Argon TPC, *JINST* **17** (01), P01005, arXiv:2108.01902 [physics.ins-det].
- [17] P. Abratenko *et al.* (MicroBooNE Collaboration), Cosmic Ray Background Rejection with Wire-Cell LArTPC Event Reconstruction in the MicroBooNE Detector, *Physical Review Applied* **15**, 10.1103/physrevapplied.15.064071 (2021).
- [18] A. A. Abud *et al.* (DUNE Collaboration), DUNE Phase II: Scientific Opportunities, Detector Concepts, Technological Solutions (2024), arXiv:2408.12725 [physics.ins-det].
- [19] M. Blennow, T. Ohlsson, and H. Snellman, Day-night effect in solar neutrino oscillations with three flavors, *Phys. Rev. D* **69**, 073006 (2004).
- [20] B. Abi *et al.* (DUNE), Deep Underground Neutrino Experiment (DUNE), Far Detector Technical Design Report, Volume II: DUNE Physics (2020), arXiv:2002.03005 [hep-ex].
- [21] A. de Gouvêa, W.-C. Huang, and J. Jenkins, Pseudodirac neutrinos in the new standard model, *Phys. Rev. D* **80**, 073007 (2009).
- [22] C. Giunti and Y. F. Li, Matter effects in active-sterile solar neutrino oscillations, *Phys. Rev. D* **80**, 113007 (2009).
- [23] K. Goldhagen, M. Maltoni, S. E. Reichard, and T. Schwetz, Testing sterile neutrino mixing with present and future solar neutrino data, *Eur. Phys. J. C* **82**, 116 (2022), arXiv:2109.14898 [hep-ph].
- [24] O. G. Miranda, M. A. Tórtola, and J. W. F. Valle, Are solar neutrino oscillations robust?, *Journal of High Energy Physics* **2006**, 008 (2006).
- [25] A. Friedland, C. Lunardini, and C. Peña-Garay, Solar neutrinos as probes of neutrino-matter interactions, *Physics Letters B* **594**, 347 (2004).
- [26] I. Esteban, M. C. Gonzalez-Garcia, M. Maltoni, I. Martinez-Soler, and J. Salvado, Updated constraints on non-standard interactions from global analysis of oscillation data, *JHEP* **08**, 180, [Addendum: *JHEP* **12**, 152 (2020)], arXiv:1805.04530 [hep-ph].
- [27] S. Gardiner, Simulating low-energy neutrino interactions with MARLEY, *Computer Physics Communications* **269**, 108123 (2021).
- [28] S. Gardiner, Nuclear de-excitations in low-energy charged-current ν_e scattering on ^{40}Ar , *Phys. Rev. C* **103**, 044604 (2021).
- [29] J. Allison *et al.*, Recent developments in Geant4, *Nuclear Instruments and Methods in Physics Research Section A: Accelerators, Spectrometers, Detectors and Associated Equipment* **835**, 186 (2016).
- [30] J. Allison *et al.*, Geant4 developments and applications, *IEEE Transactions on Nuclear Science* **53**, 270 (2006).
- [31] S. Agostinelli *et al.*, Geant4—a simulation toolkit, *Nuclear Instruments and Methods in Physics Research Section A: Accelerators, Spectrometers, Detectors and Associated Equipment* **506**, 250 (2003).
- [32] C. McGrew *et al.*, edep-sim: An Energy Deposition Simulation.
- [33] W. Castiglioni, W. Foreman, B. R. Littlejohn, M. Malaker, I. Lepetic, and A. Mastbaum, Benefits of MeV-scale reconstruction capabilities in large liquid argon time projection chambers, *Phys. Rev. D* **102**, 092010 (2020).
- [34] C. Nesaraja and E. McCutchan, Nuclear Data Sheets for A = 41, *Nuclear Data Sheets* **133**, 1 (2016).
- [35] X. Ning, W. Shi, C. Zhang, C. Riccio, and J. H. Jo, Self-compensating light calorimetry with liquid argon time projection chamber for gev neutrino physics, *Phys. Rev. D* **111**, 032007 (2025).
- [36] E. Segreto, Properties of charge recombination in liquid argon (2024), arXiv:2405.00905 [hep-ex].
- [37] F. Marinho, L. Paulucci, D. Totani, and F. Cavanna, Larql: a phenomenological model for treating light and charge generation in liquid argon, *Journal of Instrumentation* **17** (07), C07009.
- [38] J. B. Birks, Scintillations from Organic Crystals: Specific Fluorescence and Relative Response to Different Radiations, *Proceedings of the Physical Society. Section A* **64**, 874 (1951).
- [39] E. S. Tadayoshi Doke, Kimiaki Masuda, Estimation of absolute photon yields in liquid argon and xenon for relativistic (1 MeV) electrons, *Nuclear Instruments and Methods in Physics Research Section A: Accelerators, Spectrometers, Detectors and Associated Equipment* **291**, 617 (1990).
- [40] S. Amoroso *et al.*, Study of electron recombination in liquid argon with the ICARUS TPC, *Nuclear Instruments and Methods in Physics Research Section A: Accelerators, Spectrometers, Detectors and Associated Equipment* **523**, 275 (2004).
- [41] R. Acciarri *et al.*, A study of electron recombination using highly ionizing particles in the argoneut liquid argon tpc, *Journal of Instrumentation* **8** (08), P08005.
- [42] P. Abratenko *et al.* (The MicroBooNE Collaboration), Measurement of ambient radon progeny decay rates and energy spectra in liquid argon using the microboone detector, *Phys. Rev. D* **109**, 052007 (2024).
- [43] A. Abed Abud *et al.* (DUNE), The DUNE Far Detector Vertical Drift Technology. Technical Design Report,

- JINST **19** (08), T08004, arXiv:2312.03130 [hep-ex].
- [44] G. Plante *et al.*, New measurement of the scintillation efficiency of low-energy nuclear recoils in liquid xenon, Phys. Rev. C **84**, 045805 (2011).
- [45] A. Hitachi, T. Doke, and A. Mozumder, Luminescence quenching in liquid argon under charged-particle impact: Relative scintillation yield at different linear energy transfers, Phys. Rev. B **46**, 11463 (1992).
- [46] J. Thomas and D. A. Imel, Recombination of electron-ion pairs in liquid argon and liquid xenon, Phys. Rev. A **36**, 614 (1987).
- [47] Supernova Pointing Capabilities of DUNE (2024), arXiv:2407.10339 [hep-ex].
- [48] N. Van Dessel, A. Nikolakopoulos, and N. Jachowicz, Lepton kinematics in low-energy neutrino-argon interactions, Physical Review C **101**, 10.1103/physrevc.101.045502 (2020).
- [49] Impact of cross-section uncertainties on supernova neutrino spectral parameter fitting in the Deep Underground Neutrino Experiment, Phys. Rev. D **107**, 112012 (2023).
- [50] R. S. Raghavan, Inverse β^- decay of ^{40}Ar : A new approach for observing MeV neutrinos from laboratory and astrophysical sources, Phys. Rev. D **34**, 2088 (1986).
- [51] A. Priya and C. Lunardini, Diffuse neutrinos from luminous and dark supernovae: prospects for upcoming detectors at the O(10) kt scale, Journal of Cosmology and Astroparticle Physics **2017** (11), 031.
- [52] A. Abusleme *et al.* (The JUNO collaboration), Prospects for detecting the diffuse supernova neutrino background with JUNO, Journal of Cosmology and Astroparticle Physics **2022** (10), 033.
- [53] K. Abe *et al.* (Hyper-Kamiokande Proto-Collaboration), Hyper-kamiokande design report (2018), arXiv:1805.04163 [physics.ins-det].
- [54] Solar nue flux.
- [55] K. J. Kelly, P. A. N. Machado, I. Martinez-Soler, S. J. Parke, and Y. F. Perez-Gonzalez, Sub-gev atmospheric neutrinos and cp violation in dune, Phys. Rev. Lett. **123**, 081801 (2019).
- [56] R. Acciarri *et al.* (ArgoNeuT Collaboration), Demonstration of MeV-scale physics in liquid argon time projection chambers using ArgoNeuT, Phys. Rev. D **99**, 012002 (2019).